# Pulse Electrodeposition of 2.4 T $Co_{37}Fe_{63}$ Alloys at Nanoscale for Magnetic Recording Application

Stanko R. Brankovic[1], XiaoMin Yang[2], Timothy J. Klemmer[2], and Mike Seigler[2]

[1]Electrical and Computer Engineering Department, University of Houston, Houston, TX 77204-4005 USA
[2]Seagate Research Center, Pittsburgh, PA 15222 USA

**Pulse deposition of 2.4 T $Co_{37}Fe_{63}$ alloy in photoresist features with 40 nm critical dimension and high aspect ratio is presented. The design of the pulse deposition parameters is described in terms of the transport limitations through the diffusion layer, electrochemical interface stability with respect to $Fe(OH)_3$ precipitation, and the optimum conditions for additive (Saccharin) adsorption. The alloy grain size and crystal structure in the nanoconfined electrode geometry is compared versus the thin film and relevant implications for magnetic recording are discussed. The 2.4 T $Co_{38}Fe_{61}Pd_1$ alloy is introduced as a possible way to improve the corrosion properties of 2.4 T $Co_{37}Fe_{63}$ alloy.**

*Index Terms*—**Co–Fe alloys, corrosion, electrodeposition, pulse deposition, Saccharin.**

## I. INTRODUCTION

**T**HE ever-continuing drive to increase the areal density of magnetic recording inevitably brought many of the processes involved in fabrication of magnetic heads to the level of nano-science. A typical example is the fabrication of the writer's magnetic pole tip structure. Among the other processes involved in accomplishing this task, electrodeposition is facing the challenge of delivering a controlled process and properties of soft, high magnetic moment alloys into photoresist features with high aspect ratio and sub-100 nm critical dimensions (CD). For future devices with $>77$ Gbit$\cdot$cm$^{-2}$ ($>500$ Gbit$\cdot$in$^{-2}$) recording density it is predicted that these dimensions will scale down to $\sim 40$ nm in order to meet the design requirements. Fabrication of devices at this level has been enabled by the development of advanced lithography tools and processes, in particular e-beam lithography together with positive photoresist formulations [1]. The natural extension of the advances in lithography and integration with other processes on the wafer level is the implementation of the "through mask" electrodeposition on the nano-scale. This was demonstrated recently by extending the electrodeposition technology for fabrication of 1.8 T CoNiFe pole tip structures down to 50 nm CD using the pulse deposition method [2]. However, the research on new electrodeposited materials for writer applications has been inspired by an increasing need for higher saturation magnetic flux density, $(B_s)$. These efforts resulted in development of the low coercivity Co–Fe alloys, with $B_s$ values of $\sim 2.4$ T as the most probable candidate material for the future pole tip structures fabricated by electrodeposition [3], [4].

In this paper we address some of the problems that electrodeposition of soft, high magnetic moment alloys faces at the scale necessary to reach the future $>77$ Gbit$\cdot$cm$^{-2}$ magnetic recording density. Pulse deposition results for 2.4 T $Co_{37}Fe_{63}$ alloy in nanoconfined photoresist geometries, for pole tip fabrication, are presented as an illustration of the effectiveness of our approach. The design of the pulse deposition parameters is discussed in terms of the transport limitations through the diffusion layer, electrochemical interface stability with respect to $Fe(OH)_3$ precipitation, and the optimum conditions for additive (Saccharin) adsorption at the $Co_{37}Fe_{63}$ surface. The comparative analysis of the $Co_{37}Fe_{63}$ alloy grain size and crystal structure in the pole tip configuration, versus $Co_{37}Fe_{63}$ alloy thin film is made, and relevant implications for magnetic recording are discussed. One of the possible ways to improve the corrosion properties of 2.4 T $Co_{37}Fe_{63}$ is presented through the introduction of 2.4 T $Co_{38}Fe_{61}Pd_1$ alloy.

## II. EXPERIMENTAL PROCEDURE

The cell configuration and geometry used in this study have been described previously, [5], [6]. All samples used in this study were 6-in AlTiC wafers with a 100 nm Ru or Cu seed. The photoresist patterning required to obtain the nanoelectrode geometry suitable for the pole tip deposition studies was produced using advanced e-beam lithography and a subsequent photoresist annealing procedure [1]. The background solution was a modified Watt's electrolyte containing $H_3BO_3$ and $NH_4Cl$ as a buffers. The pH of the solution was adjusted with diluted $H_2SO_4$. Metal ions in the solution were obtained by dissolution of the proper amounts of $CoSO_4 \cdot 7H_2O$ and $FeSO_4 \cdot 7H_2O$. The additive used in the deposition experiments was Saccharin. Differential capacitance measurements were obtained on electrodeposited $Co_{37}Fe_{63}$ surface using modulation amplitude of 5 mV at a frequency of 400 Hz. All corrosion measurements were done in 0.5 M NaCl solution. The potentials of the electrode surface in this work are quoted versus the saturated calomel electrode (SCE). The composition of the Co–Fe samples was verified by energy dispersive X-ray spectroscopy (EDX) and secondary ion mass spectroscopy (SIMS).

## III. DESIGN OF THE PULSE DEPOSITION PARAMETERS

Pole tip depression (Fig. 1) has been recognized as the limitation of the traditionally used direct current (dc) electrodeposition method as the critical dimensions of the pole tip structures
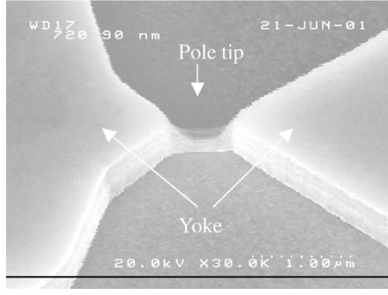
Fig. 1.   Secondary electron image of the pole tip depressions. The yoke and pole tip regions are indicated with arrows.
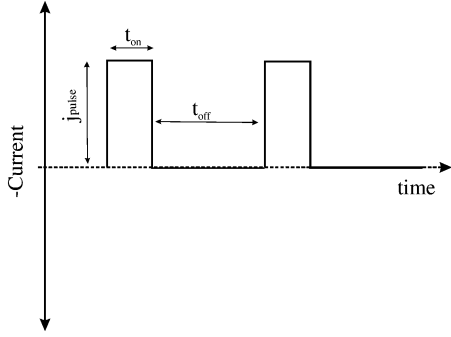


Fig. 2.   Pulse deposition function profile. The parameters $t_{\rm on}, t_{\rm off}$, and $j_{\rm pulse}$ are indicated in the figure.

approached $<100$ nm level. This phenomenon is caused by a lower deposition rate in the narrow photoresist pole tip features as compared to the larger yoke structures. Different mechanisms could be associated with the hindered deposition in the pole tip region, depending on the specifics of the plating solution and additive design, process parameters, and CDs of the pole tip electrode geometry. The alternatives to dc deposition process, pulse deposition (PD) and pulse reverse deposition (PRD) [7], have already been proven very effective for electrodeposition of magnetic alloys [8]–[10]. These methods were shown to be capable of depositing magnetic materials in templates with sub-100 nm dimensions [11], as well as producing electrodeposits with very smooth surfaces [12], and ultra-small grain size [13].

The pulse current function that we employed in our work has a simple ON/OFF profile shown in Fig. 2. The successful application of this pulse function is dependent on proper determination of the pulse time $t_{\rm on}$, rest time $t_{\rm off}$, and magnitude of the pulse current density $j_{\rm pulse}$. These parameters could be defined through the tedious trial and error experiments or using some of the generalized mathematical models adapted for particular solution chemistry, electrode size, and geometry. In the following text, we will discuss our approach for the design of pulse parameters for electrodeposition of 2.4 T Co$_{37}$Fe$_{63}$ alloy in high aspect ratio pole tip structures with the CD of $\sim$40 nm that is necessary for the future high recording density devices.

## A.  Duration of the Pulse Current Stage $(t_{\rm on})$

In order to determine the optimum duration of the pulse current stage, limitations for ion transport toward the electrode-electrolyte interface need to be taken into account. When Co–Fe

electrodeposition is considered, several approximations and assumptions should be emphasized.

1) The transport through the diffusion layer is the dominant phenomenon and electro-migration and convection contributions to the transport are neglected.
2) In the case of our solution chemistry, the concentrations of metal ions are larger than the concentration of hydrogen ions, $[M^{n+}] \gg [H^+]$, and for very low current efficiency, $\gamma$, it is assumed that depletion of the hydrogen at the interface occurs prior to the metal ions encountering any transport limiting conditions during the pulse current stage.
3) The formation of insoluble Fe(OH)$_3$ precipitate is assumed to be the main reason for hindered deposition at the Co–Fe surface, in particular in the region of the pole tip. This assumption is the related to the presence of Fe$^{3+}$ ions in the aerated solutions containing Fe$^{2+}$ ions. The Fe$^{3+}$ ions are generated as product of the oxidation of Fe$^{2+}$ ions by dissolved oxygen in the solution $(O_2 + 4Fe^{2+} + 4H^+ \rightarrow 4Fe^{3+} + 2H_2O)$ and by electrochemical oxidation of Fe$^{2+}$ at the anode surface during the electrodeposition process.

The mathematical treatment of the ion diffusion problem through the Nernst diffusion layer during the galvanostatic pulse means solving Fick's second law of diffusion with appropriate boundary conditions. Since the hydrogen ions are the ones to consider, the appropriate formulation of the problem is presented in (1)

$$\frac{\partial C^{H^+}}{\partial t} = D^{H^+} \cdot \frac{\partial^2 C^{H^+}}{\partial x^2}. \tag{1}$$

In the above expression, $D^{H^+}$ is the diffusion coefficient for hydrogen ions in the solution. The initial conditions for this problem are defined as follows:

$$t = 0; \quad {\rm x} \geq 0, \quad {\rm C}^{H^+} = C_\infty^{H^+} \quad ; {\rm x} \geq \delta, \quad {\rm C}^{H^+} = C_\infty^{H^+} \tag{2}$$

where $C_\infty^{H^+}$ and $\delta$ are the $H^+$ concentration in the bulk of the solution and the diffusion layer thickness, respectively. The boundary conditions at the interface after the application of the current pulse are

$$t > 0, \quad x = 0; \quad \frac{\partial C^{H^+}}{\partial x} = -\frac{(1 - \gamma) \cdot j_p}{F \cdot D_{H^+}} = {\rm const.},$$
$$t > 0, \quad x = 0; \quad C^{H^+} = C_i^{H^+}. \tag{3}$$

The terms $C_i^{H^+}, j_p, \gamma$, and $F$ stand for the $H^+$ concentration at the interface, current density of the pulse, current efficiency, and Faraday's constant, respectively. The exact mathematical solution of this problem is somewhat cumbersome, presented in the form of a Fourier series expansion [14]. For practical application, it is more convenient to consider approximate solutions that are dependent on the value of the term $a \cdot t$, where $a$ is defined as

$$a = \frac{\pi^2 D^{H^+}}{4\delta^2}. \tag{4}$$

TABLE I
PARAMETERS USED IN CALCULATIONS

| Symbol | Value | Unit | Reference |
|---|---|---|---|
| $\delta$ | $35 \cdot 10^{-4}$ | cm | [16] |
| $D^{H^+}$ | $9.3 \cdot 10^{-5}$ | cm$^2$·s$^{-1}$ | [15] |
| $K_{Fe(OH)3}$ | $3.2 \cdot 10^{-38}$ | mol$^4$ lit$^{-4}$ | [17] |
| $K_{H2O}$ | $10^{-14}$ | mol$^2$ lit$^{-2}$ | [18] |
| $\gamma$ | 0.1 | - | Experiment |
| $F$ | 96,485 | C·mol$^{-1}$ | [18] |

The evaluation of this term is dependent on an appropriate estimate of $D^{H^+}$ and $\delta$. The data for these parameters are readily available in the literature [15], [16] or could be measured experimentally for a particular experimental setup. The values we used for our calculations are summarized in Table I.

For moderately short pulse times, $t > 0.01$ s, the value of $a \cdot t$ is greater than 0.2, which allows us to use the approximate form of the solution for (1) with accuracy better than 1%, (5), [14]

$$C_i^{H^+} = C_\infty^{H^+} - \frac{(1-\gamma) \cdot j_p \cdot \delta}{F \cdot D^{H^+}}$$
$$\cdot \left\{ 1 - \frac{8}{\pi^2} \cdot \exp\left( -\frac{\pi^2 \cdot D^{H^+}}{4\delta^2} \cdot t \right) \right\}. \quad (5)$$

To use this equation for the estimate of the pulse duration, we have to define the concentration of H$^+$ at the interface and solve the equation explicitly for $t$. According to the assumption we made, the maximum duration of the pulse stage, $\tau$, is defined by formation of the conditions allowing the precipitation of Fe(OH)$_3$ at the interface. This happens when the concentration of the OH$^-$ ions exceeds the level defined by the Fe(OH)$_3$ product of solubility, (6)

$$\left[ C_\infty^{Fe^{3+}} \right] \cdot \left[ C_i^{OH^-} \right]^3 \geq K_{Fe(OH)_3}. \quad (6)$$

Defining this condition, we assume that the Fe$^{3+}$ does not participate directly in the electrodeposition process and its concentration at the interface is assumed to be the same as in the bulk. Because of that, our estimate for the duration of the pulse stage is presented as a function of the concentration of Fe$^{3+}$ in the bulk solution ($C_\infty^{Fe^{3+}}$).

The concentration of OH$^-$ ions at the interface is a direct function of the concentration of the H$^+$ at the interface, through the relation defining the ionic product of water

$$K_{H_2O} = C_i^{H^+} \cdot C_i^{OH^-}. \quad (7)$$

Combining (6) and (7), we can express the minimum allowed concentration of H$^+$ at the interface at the end of the pulse stage as a function of the Fe$^{3+}$ ion concentration in the bulk solution as

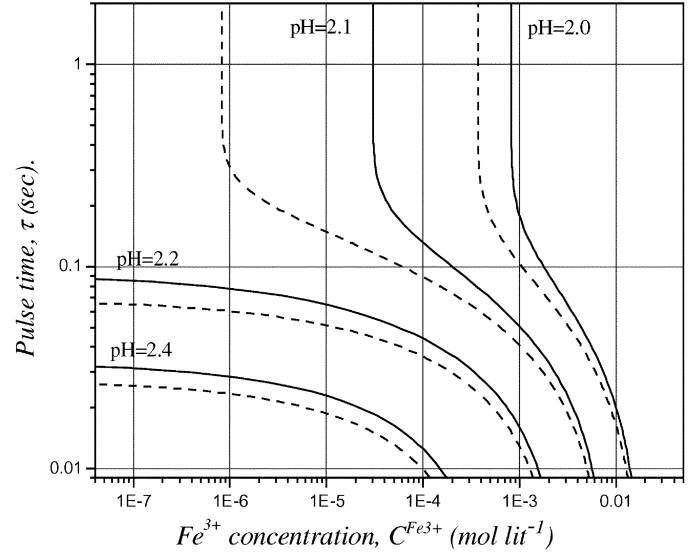$$C_i^{H^+} = \sqrt[3]{\frac{K_{H_2O}^3}{K_{Fe(OH)_3}} \cdot C_\infty^{Fe^{3+}}}. \quad (8)$$



Fig. 3. Maximum duration of the pulse stage, $\tau$, (9) as a function of the Fe$^{3+}$ concentration in the solution. The dependence is presented for four different pH values of the solution and two pulse current densities, 20 mA·cm$^{-2}$ (solid line) and 22 mA·cm$^{-2}$ (dashed line). The other parameters used in calculation are summarized in Table I.

Substituting (8) into (5) and presenting $C_\infty^{H^+}$ as $10^{-pH}$ the final expression for the maximum duration of the pulse current stage $\tau$ as a function of the $C_\infty^{Fe^{3+}}$ is defined as

$$\tau = -\frac{4\delta^2}{\pi^2 D^{H^+}}$$
$$\cdot \ln \left\{ \frac{\pi^2}{8} \cdot \left( 1 - \frac{F \cdot D^{H^+} \cdot \left[ 10^{-pH} - \sqrt[3]{\frac{K_{H_2O}^3}{K_{Fe(OH)_3}} \cdot C_\infty^{Fe^{3+}}} \right]}{(1-\gamma) \cdot j_p \cdot \delta} \right) \right\}. \quad (9)$$

The predictions of (9) are plotted in Fig. 3 for different pH values of the solution and two different pulse current densities. The pulse time duration estimate is presented only for the values larger than 0.01 s because for shorter pulse times the accuracy of the approximate solution (5) is not satisfactory to better than 1%.

It is worthwhile to look at some practical implications of the results in Fig. 3. For given pulse current densities, sufficiently high concentration of H$^+$ (low pH) and low concentration of Fe$^{3+}$ in the solution, it is predicted that the interfacial concentration of the H$^+$ ions will never reach the value required to form hydroxide precipitate, even for very long pulse times. However, this is rarely the case in practice since the aerated solutions with high content of Fe$^{2+}$ ions inevitably have significant presence of Fe$^{3+}$ too. For the design of the pulse time interval $t_{on}$, the general rule is to have the length of the pulse shorter than the maximum one estimated by (9)

$$t_{on} < \tau. \quad (10)$$

From Fig. 3, it is obvious that a small variation in pH of the solution can significantly affect the allowed duration of the pulse stage. For example, for a $10^{-3}$ mol·lit$^{-1}$ concentration of Fe$^{3+}$, and pulse current density of 20 mA·cm$^{-2}$ the increase in the pH

of the solution of ~5% (from 2 to 2.1) leads to a decrease of the $\tau$ of more than 300%. Knowing that, in the real situation, a 5% variation in pH is considered very possible, one can anticipate a significant restriction of the $t_{on}$ as compared to the estimated value of $\tau$. Another useful way of interpreting these results is to look at the variation of $\tau$ with an increasing pulse current density. For the same concentration of $Fe^{3+}$, but for an increase of 10% in $j_p$, the value of $\tau$ decreases by ~40%. This is important when considering the geometrical and secondary current distribution [19] effects on the through-mask electrodeposition process of nanoscale features. A significant variation of the local current density $j_l$ to the applied (average) pulse current density $j_p$ within the pole tip electrode geometry could add an additional constraint on the values of $t_{on}$ as compared to the estimated ones.

### B. Duration of the Rest Time $(t_{off})$

The rest time of the pulse is defined in terms of the time that is necessary to recover the concentration of $H^+$ ions at the solution-electrode interface to some arbitrary fraction of the starting value prior to the current pulse. In order to mathematically define this situation we consider the diffusion of $H^+$ ions through the layer of thickness $\delta$ from the bulk of the electrolyte to the electrode-solution interface defined by (1).

The initial and boundary conditions are defined as

$$
\begin{aligned}
t = 0; & \quad x = 0, \quad C^{H^+} = C_{i0}^{H^+}, \quad \text{and } x = \delta, \quad C^{H^+} = C_\infty^{H^+} \\
t > 0; & \quad x = 0, \quad C^{H^+} = C_i^{H^+}, \quad \text{and } x = \delta, \quad C^{H^+} = C_\infty^{H^+}.
\end{aligned}
\tag{11}
$$

The driving force for diffusion flux in this case is the concentration gradient across the diffusion layer of thickness $\delta$, and is assumed to be linear

$$
\begin{aligned}
t = 0; & \quad \frac{\partial C^{H^+}}{\partial x} = \frac{C_\infty^{H^+} - C_{i0}^{H^+}}{\delta}, \quad \text{and} \\
t > 0; & \quad \frac{\partial C^{H^+}}{\partial x} = \frac{C_\infty^{H^+} - C_i^{H^+}}{\delta}.
\end{aligned}
\tag{12}
$$

The solution of this problem has an exponential form, where the $H^+$ ion concentration at the interface $(x = 0)$ asymptotically approaches the value of $C_\infty^{H^+}$

$$
C_i^{H^+} = C_\infty^{H^+} + \left( C_{i0}^{H^+} - C_\infty^{H^+} \right) \cdot \exp \left( -\frac{2D^{H^+}}{\delta^2} \cdot t \right).
\tag{13}
$$

If we assume that the rest time, $t_{off}$, should be long enough to recover the $H^+$ concentration to 99% of its bulk value, $(C_i^{H^+}/C_\infty^{H^+} = 0.99)$, and expressing $C_{i0}^{H^+}$ in terms of (8), as well as presenting $C_\infty^{H^+}$ as $10^{-pH}$, the final form for the rest time, $t_{off}$, as a function of $Fe^{3+}$ concentration and pH in the solution can be written as

$$
t_{off} = \frac{\delta^2}{2D^{H^+}}
$$
$$
\cdot \left\{ \ln \left[ 1 - \sqrt[3]{\frac{K_{H_2O}^3}{10^{-(3 \cdot pH)} \cdot K_{Fe(OH)_3}} \cdot C_\infty^{Fe^{3+}}} \right] + 4.60 \right\}.
\tag{14}
$$



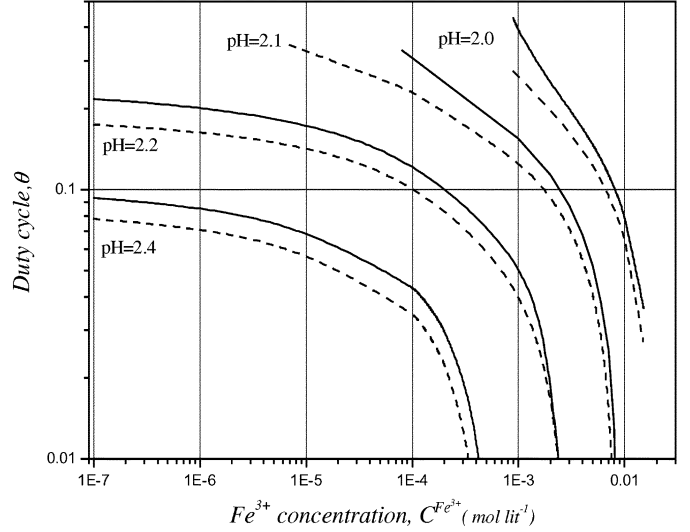Fig. 4. Values of duty cycle $\theta$ (15) as a function of the $Fe^{3+}$ concentration in the solution, four different pH values of the solution and two pulse current densities, 20 mA·cm$^{-2}$ (solid line) and 22 mA·cm$^{-2}$ (dashed line). Parameters used in the calculation are summarized in Table I.

Inspection of (14) indicates that for some very low concentrations of $Fe^{3+}$ in the solution, $Fe^{3+} \to 0$, $t_{off}$ is almost constant ~0.31 s. For values of $Fe^{3+}$ closely approaching the solubility limit for given pH of the solution, $t_{off}$ is rapidly decreasing to very small impractical values.

For practical purposes, it is useful to discuss the predictions of (14) in conjunction with (9) through the parameter often called the "*duty cycle*" $(\theta)$, defined as

$$
\theta = \frac{t_{on}}{t_{on} + t_{off}} < \frac{\tau}{\tau + t_{off}}.
\tag{15}
$$

A plot of $\theta$ as a function of $Fe^{3+}$ concentration, for two different pulse current densities and different pH of solutions, is shown in Fig. 4. The $\theta$ values are presented as an upper limit defined by the right side of (15). One can see that $\theta$ has a decreasing trend as the concentration of $Fe^{3+}$ in the solution and pH are increasing. Assuming that the condition defined by (15) is fulfilled, the appropriate values of $\theta$ that should be used are smaller than the ones plotted in Fig. 4. The effect of the pulse current density on $\theta$ is also important, as we mentioned discussing the results of (9). However, the sensitivity of this estimate on pulse current density is not the same as observed for $\tau$. This effect is particularly small as the $Fe^{3+}$ concentration is approaching the solubility limit, whereas for the very low $Fe^{3+}$ concentrations it is reflected as ~20% increase for ~10% higher $j_p$.

### C. Magnitude of the Pulse Current Density

In the previous discussion regarding the definition of $\tau$ we used an arbitrary pulse current density for the estimate. To present a more elaborate discussion about this important parameter one would need to look at the potential range where maximum additive adsorption occurs on the Co–Fe electrode surface. The benefit that additives offer in the electrodeposition process is fully realized only if the electrode surface, during the electrodeposition process, is in the potential range where maximum additive coverage is expected. This effect has already
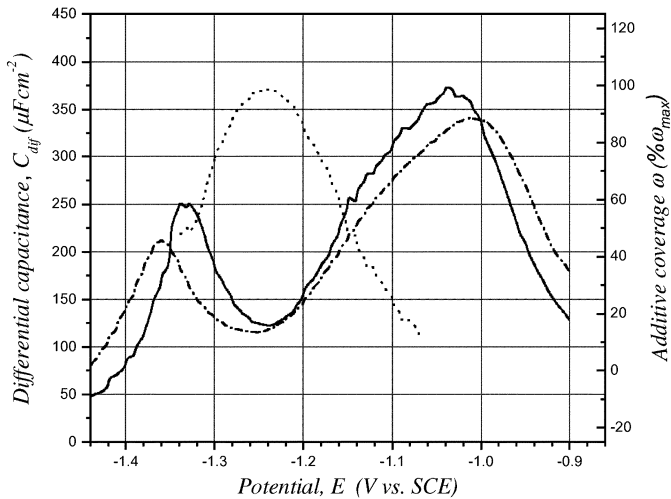
Fig. 5. Differential capacitance measurements on a $Co_{37}Fe_{63}$ surface for 0.25 g·lit$^{-1}$ (solid line) and 1.0 g·lit$^{-1}$ (dashed line) concentrations of Saccharin in solution. The apparent Saccharin coverage in the potential range of condensed film formation for solution with 0.25 g·lit$^{-1}$ is presented with dotted line referring to the right ordinate.

been demonstrated for pulse electrodeposition of 1.8 T CoNiFe alloys [20] in 50 nm CD pole tip photoresist features and, following the same logic, the pulse current design procedure is presented here.

Saccharin is the most common additive used in the electrodeposition of Co–Fe alloys. The differential capacitance measurement on 2.4 T $Co_{37}Fe_{63}$ surfaces, in solutions containing different concentration of Saccharin is presented in Fig. 5. The typical capacitance well observed in the potential region between $-1.05$ and $-1.35$ V is characteristic of the adsorption of organic additives on a transition metal electrode surface. The minimum of the capacitance well is around $-1.25$ V, and as the concentration of the Saccharin is increased four times, the minimum of the capacitance well broadens out for about 0.05 V. This is an indication that some form of Saccharin condensed film exists on the $Co_{37}Fe_{63}$ surface [21].

The apparent coverage of the Saccharin-adsorbed phase in the range of the capacitance well can be estimated using the following expression [21]:

$$\varpi_{app} = \frac{C_{max} - C}{C_{max} - C_{min}} \cdot 100\%. \qquad (16)$$

Here, $C_{max}$ and $C_{min}$ represent the maximum and minimum values of the differential capacitance within the capacitance well. The Saccharin surface coverage, for concentration of 0.25 g·lit$^{-1}$, is presented in Fig. 5 with a dotted line. Considering these results, the optimum pulse current used in the deposition process would be the one where the potential of the electrode surface rests at approximately $-1.25$ V during the pulse stage. To illustrate this, Fig. 6 shows the surface morphology of the $Co_{37}Fe_{63}$ pole tip test structures electrodeposited with two different pulse current densities and having different potentials of the electrode surface. The pulse function parameters $t_{on}$ and $t_{off}$ in each case are estimated using the procedure previously described for a given pulse current density (18 mA·cm$^{-2}$ and 25 mA·cm$^{-2}$). The estimated Saccharin coverage of the surface during the pulse stage in image A is $\sim$95%,
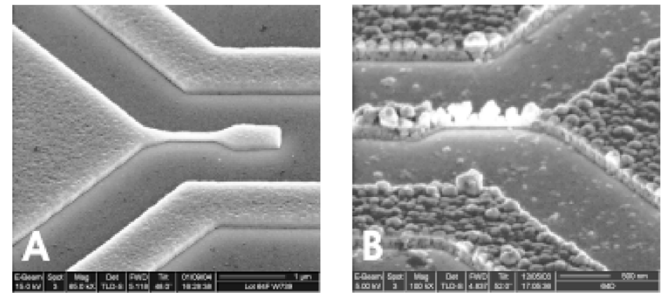


Fig. 6. $Co_{37}Fe_{63}$ pole tip test structures for two different pulse currents; (A) $j_p = 18$ mA·cm$^{-2}$, E$\sim -1.24$ V,(B) $j_p = 25$ mA·cm$^{-2}$ E$\sim -1.35$ V.
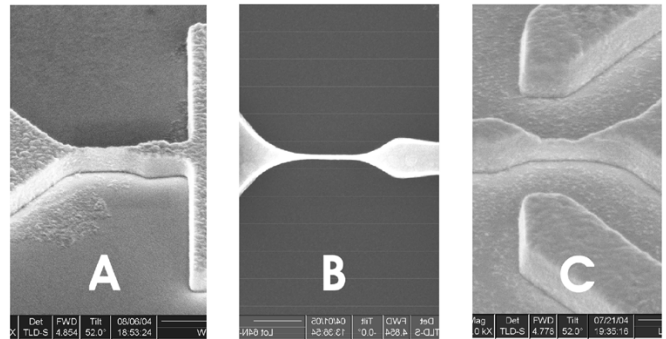


Fig. 7. $Co_{37}Fe_{63}$ pole tip test structure with high aspect ratio produced from the solution with pH $= 2.1$ containing $10^{-3}$ mol Fe$^{3+}$. (A) Side view, $\alpha = 52°$, dimensions: height $= 500$ nm, length $= 600$ nm and width $= 40$ nm, $50\,000\times$. (B) Top view of structure in image A, $80\,000\times$. (C) Side view, $\alpha = 52°$, of the structure with pole tip depression, $80\,000\times$.

whereas for image B it is $\sim$30%. Saccharin concentration in each case is the same, 0.25 g·lit$^{-1}$. The surface morphology in these two images differs significantly, indicating the importance of the additive adsorption and coverage during the pulse stage for obtaining the optimum pulse deposition results. Using pulse current densities at which the potential of the electrode surface allows the additive condensed film formation provides the opportunity to use the minimal concentration of additives in the solution, while still obtaining the excellent results. By using the pulse current regime where the potential of the $Co_{37}Fe_{63}$ surface was $\sim -1.25$ V, we were able to obtain very good pulse deposition results even with Saccharin concentrations of 0.1 and 0.05 g·lit$^{-1}$.

The method for designing the pulse parameters that we described here has been shown as accurate and very effective for fabrication of $Co_{39}Fe_{63}$ nanostructures. As an illustration, in Fig. 7, a 12:1 aspect ratio 2.4 T $Co_{37}Fe_{63}$ pole tip structures are presented. Fig. 7(A) and (B) show one of the $12\,000$ structures produced on the wafer level in one electrodeposition operation, with typical yield better than 90%. The pulse deposition parameters used to produce these two structures are estimated by previously described procedure. The CD of the narrow part of pole tip is $\sim$40 nm, which is sufficient for recording densities above 77 Gb·cm$^{-2}$. The surface roughness across the pole tip region is less than 2 nm, which represents only 0.4% variation in thickness of the pole tip. In Fig. 7(C), for comparison purpose, a pole tip structure with CD $\sim$65 nm is presented. This structure is produced by same pulse current density as structure in Fig. 7(A) and (B) but with pulse parameter $t_{on}$ being longer
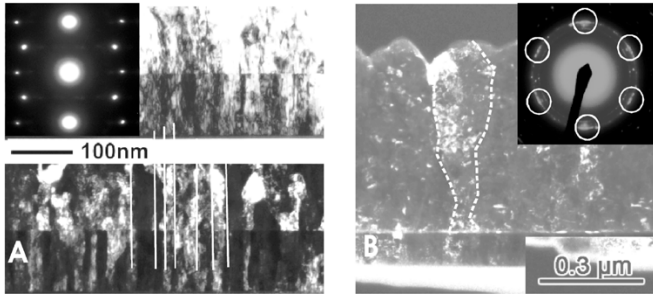
Fig. 8. TEM images for Co$_{37}$Fe$_{63}$ alloy in thin film (A) and pole tip (B) geometry. Insets on each image represent the TEM-X ray diffraction pattern. The solid and dotted lines on the images are drawn to guide the eye over the grain boundaries and diffraction peaks.

than estimated by (9). As a consequence, the allowed formation of Fe(OH)$_3$ during the pulse stage has hindered the deposition in the pole tip region yielding the overall pole tip depression profile.

## IV. CRYSTAL STRUCTURE OF THE 2.4 T Co$_{37}$Fe$_{63}$ DEPOSIT IN THE POLE TIP GEOMETRY

The Co$_{37}$Fe$_{63}$ thin films produced by pulse electrodeposition on Ru seed had a BCC crystal structure with predominant $\langle 110 \rangle$ fiber texture. The grain shape was developed as columnar structure with lateral dimensions of approximately $\sim$10–20 nm, starting from the initial Ru seed. A representative Transmission Electron Microscopy (TEM) image and corresponding TEM-X ray diffraction pattern are presented in Fig. 8. In the diffraction pattern of Fig. 8(A) it is important to notice that all (110) diffraction peaks characteristic of a BCC $\langle 110 \rangle$ fiber texture are present in the diffraction pattern indicating full freedom of the in-plane grain rotation. Additionally, the diffraction pattern is composed of spots and not arcs indicating a very tight distribution of out-of-plane dispersions. For this type of sample, the characterization of the magnetic properties shows the $B_s$ value of 2.43 T and coercivity value measured along the easy axis of $\sim$4 Oe. The characterization of magnetic properties for the alloy in the pole tip geometry at this moment is not possible with conventional equipment and existing techniques. In order to be able to make a qualitative comparison, the TEM inspection of the representative sample for pole tip geometry is done. The sample is produced by pulse electrodeposition in a 20 $\mu$m long strip of $\sim$50 nm CD that was subsequently undercut from the wafer base by a focused ion beam. The result is presented in image B in Fig. 8. The most appealing difference is that, for the pole tip sample, the grain shape and lateral grain size are significantly different than for the thin film (Fig. 8).

Starting from the interface, the grain size for the pole tip sample gradually increases, which contributes to the overall hybrid type of the grain structure. The size of the grains at the upper edge of the sample of 0.6-$\mu$m thickness is almost 200 nm in width. There are two main differences when comparing the diffraction pattern of Fig. 8(A) to (B). First of all the out-of-plane tilting dispersions are clearly larger in the patterned structure, which is indicated by arcs in the pattern. It is not believed that the FIB process created this as an artifact but it cannot

be completely ruled out. The second difference is that the 90° diffraction peak is missing, which is, in the TEM setup configuration, the ($1\bar{1}0$) plane parallel to the incident electron beam. Although this peak is inherently relatively weak, we would expect to see more relative intensity than what is observed. This would mean that the ($1\bar{1}0$) is biased parallel to the plane we are viewing and that the fiber texture is therefore not complete. Indirectly, we can conclude that one-grain orientation is dominating, at least for the grains facing the resist walls, and defining the sample shape. A possible scenario for development of this structure could be that the growth of the grains with the ($1\bar{1}0$) low surface energy plane facing the resist walls is thermodynamically favored whereas the other grain orientations gradually die out as the thickness of the deposit increases. Having the size of the electrode approaching the thickness of the grains, the contribution of these surface grains becomes dominant to the overall crystallographic texture of the pole tip. Since the magnetic anisotropy depends on this texture, and the magnetic softness is dependent on an average grain size [22], the logical question would be how the magnetic properties of the Co$_{39}$Fe$_{63}$ alloy in the pole tip geometry differ from the ones that we know for thin films. To answer this question, more experimental work and modeling efforts are needed.

## V. IMPROVING THE CORROSION PROPERTIES OF 2.4 T Co$_{37}$Fe$_{63}$ ALLOY

The poor corrosion resistance of electrodeposited 2.4 T Co$_{37}$Fe$_{63}$ alloy seriously compromises its benefit of having high magnetic moment and desirable magnetic softness. This problem is related to the electrochemical nature of the Co and Fe elemental constituents of the alloy, and its low corrosion resistance is expected from the general corrosion theory and other data known in related literature [23]. Unlike other soft magnetic alloys with significant content of Ni (Co–Fe–Ni or Permalloy), the dominant content of Fe and lack of Ni in the case of Co$_{37}$Fe$_{63}$ deposit are the major reasons for its inability to form a stable passive film and to have satisfactory corrosion properties. The straightforward way to improve this situation is to add a small amount of an additional noble metal into the alloy. The physical concept behind adding the noble metal into the alloy is to increase the absolute value of the work function and to slightly modify the electron structure. As a consequence, the increase of the energy barrier for the charge transfer during the electrochemical oxidation of the metal surface is expected, yielding the lower corrosion rates. Looking at the periodic table, using one of the Pt group metals for alloying with the Co$_{37}$Fe$_{63}$ alloy would be the natural choice. However, the addition of a nonmagnetic noble metal into the ferromagnetic matrix would also reduce the value of $B_s$. Based on this fact, several noble metal candidates were considered. As a result of our electronic structure and atomic magnetic moments calculations, using local spin density functional theory, with generalized gradient correction employing projected augmented waves method [24], Pd and Rh were selected as the most effective choices. Here we will discuss the example of Pd alloying with 2.4 T Co$_{37}$Fe$_{63}$, yielding the 2.4 T Co$_{38}$Fe$_{61}$Pd$_1$ alloy with improved corrosion resistance.
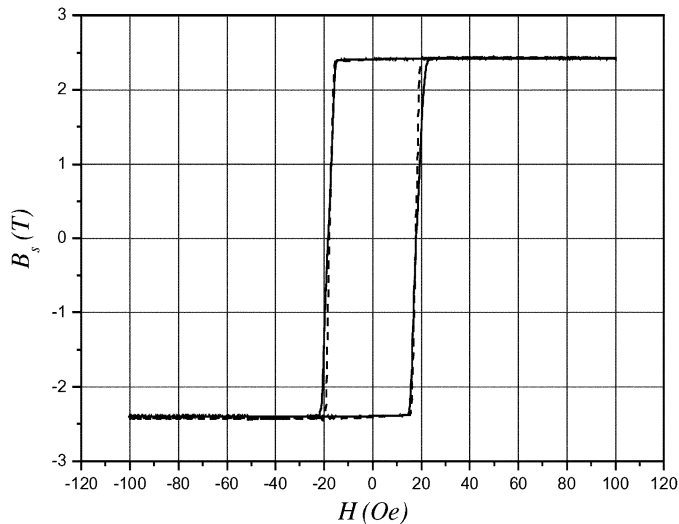
Fig. 9.  $Co_{37}Fe_{63}$ (dashed line) and $Co_{38}Fe_{61}Pd_1$ (solid line) magnetic hysteresis loops for easy axis. The samples are electrodeposited on a (111) textured Cu seed.



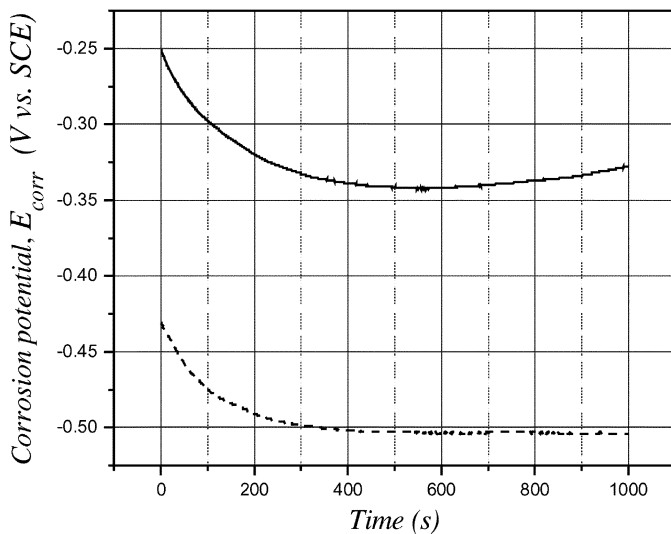Fig. 10.  Corrosion potential transients for $Co_{37}Fe_{63}$ (dashed line) and $Co_{38}Fe_{61}Pd_1$ (solid line) alloys in 0.5 M NaCl solution.

Fig. 9 shows the magnetic hysteresis loop for the easy axis of pulse electrodeposited 2.4 T $Co_{37}Fe_{63}$ and 2.4 T $Co_{38}Fe_{61}Pd_1$ alloys. The Pd content in the second alloy is obtained by adding the appropriate amount of $PdCl_2$ salt in the solution used for electrodeposition of $Co_{37}Fe_{63}$. The data are almost indistinguishable for these two alloys. The measured $B_s$ values are in the range of 2.41–2.43 T, and they are the same within the error bar of the measurements (5%), for both alloys. The only difference that could be noticed is the slight increase of the coercivity measured along the easy axis, ~18 Oe for the $Co_{38}Fe_{61}Pd_1$ versus ~17 Oe for the $Co_{37}Fe_{63}$ alloy. We conclude that 1 at% of Pd addition into the magnetic alloy did not result in any measurable deterioration of the magnetic properties.

Investigation of the corrosion resistance is somewhat a complex task, but the first screening point in order to see if there is a qualitative difference between these two alloys is to look at the corrosion potential transients. The results are presented in Fig. 10. The shift of corrosion potential in the anodic direction of approximately 0.15 V is a good indication of a benefit of Pd

presence in $Co_{38}Fe_{61}Pd_1$ and an increased nobility of the surface as compared to $Co_{37}Fe_{63}$ alloy.

Our cyclic voltammetry and impedance measurements (data not shown here) also indicate the increased corrosion resistance in $Co_{38}Fe_{61}Pd_1$. The electro-oxidation potential of $Co_{38}Fe_{61}Pd_1$ surface was shifted by approximately 0.17 V in the anodic direction, and the charge transfer resistance was measured to be six times higher than the $Co_{37}Fe_{63}$ alloy. The increased charge transfer resistance could be linked directly to the lower corrosion rate of this alloy, which was the main intention of our work on Pd alloying.

The assessment of the potential benefit of this type of alloys for integration in the future magnetic recoding devices is yet to be seen, and it would require a full scale developing effort and thin film head build. We believe that positive results demonstrating the improved corrosion resistance of $Co_{38}Fe_{61}Pd_1$ alloy in thin film configuration are likely to be extended down to the very level of the pole tip structures. However, the additional issues like different alloy crystal structure in the pole tip geometry versus the thin film configuration demonstrated previously, the high surface curvature, and other effects that are potentially relevant at nanoscale could additionally influence the corrosion behavior of this alloy at the device level on either positive or negative way.

## VI. Conclusion

The electrodeposition of soft, high magnetic moment alloys has been widely used as one of the key fabrication processes in manufacturing of magnetic recording heads for almost three decades [3]. The desire for higher magnetic moment electrodeposited materials, and the necessity of delivering magnetic structures with at least one dimension in the range of several tens of nanometers, are new challenges that need to be addressed for future high density recording devices. In this paper, we demonstrated that electrodeposition is an extendible technology for 2.4 T $Co_{37}Fe_{63}$ pole tip fabrication down to the 40 nm level, using the pulse deposition method. This complex challenge is addressed successfully by fully considering the conditions at the electrochemical interface for additive adsorption, iron hydroxide formation, and recovery of the initial conditions before the pulse current stage. An additional aspect of the electrodeposition in the nanoconfined electrode geometry is demonstrated through the results indicating a different grain structure of the deposit in the pole tip versus the thin film sample geometry. This problem will surely deserve more attention and research efforts in the future in order to have an appropriate assessment of the possible implications for the magnetic recording process. One of the factors that will be dominant in enabling the integration of Co–Fe electrodeposited alloys in the future recording heads is their corrosion resistance. We have demonstrated one of the possible ways to address this problem through the introduction of 2.4 T $Co_{38}Fe_{61}Pd_1$ alloy with improved corrosion properties. The work on other solutions for this problem undoubtedly will be one of the main research directions in the near future in terms of development of new electrodeposited materials for magnetic recording applications.

## REFERENCES

[1] X. Yang, H. Gentile, A. Eckert, and S. R. Brankovic, "Electron-beam SAFIER™ process and its application for magnetic thin film heads," *J. Vac. Sci. Technol. B*, vol. 22, pp. 3339–3343, Nov./Dec. 2004.

[2] S. R. Brankovic, K. Sendur, T. J. Klemmer, X. Yang, and E. C. Johns, "Pulse plating of soft high magnetic moment materials—Properties and application," in *Magnetic Materials, Processes, and Devices VII and Electrodeposition of Alloys*, S. Krongelb, L. T. Romankiw, J.-W. Chang, Y. Kitamoto, J. W. Judy, C. Bonhote, G. Zangari, and W. Schwarzacher, Eds. Pennington, NJ: The Electrochemical Society, 2003, PV2002-27, pp. 269–280.

[3] E. I. Cooper, C. Bonhote, J. Heidman, Y. Hsu, P. Kern, J. W. Lam, M. Ramasubramanian, N. Robertson, L. T. Romankiw, and H. Xu, "Recent development in high-moment electroplated materials for recording heads," *IBM J. Res. Dev.*, vol. 49, pp. 103–126, Jan. 2005.

[4] T. Osaka, T. Yokoshima, D. Shiga, K. Imai, and K. Takashima, "A high moment CoFe soft magnetic thin film prepared by electrodeposition," *J. Electrochem. Soc.*, vol. 6, pp. C53–C55, Jan. 2005.

[5] J. V. Powers and L. T. Romankiw, U.S. Patent 3 652 442, 1972.

[6] M. Datta and D. Landolt, "Fundamental aspects and applications of electrochemical microfabrication," *Electrochem. Acta*, vol. 45, pp. 2535–2558, Jan. 2005.

[7] J. C. Puippe and F. Leaman, *Theory and Practice of Pulse Plating*: AESF, 1986.

[8] B. N. Popov, K.-M. Yin, and R. E. White, "Galvanostatic pulse and pulse reverse plating of nickel-iron alloys from electrolytes containing organic compounds on a rotating disk electrode," *J. Electrochem. Soc.*, vol. 140, pp. 1321–1330, 1993.

[9] D. L. Grimmett, M. Schwartz, and K. Nobe, "A comparison of dc and pulsed Fe-Ni alloy deposits," *J. Electrochem. Soc.*, vol. 140, pp. 973–978, 1993.

[10] N. H. Phan, M. Schwartz, and K. Nobe, "Pulsed deposition of Fe-Ni-Co alloys," *Electrochim. Acta.*, vol. 39, pp. 449–453, 1994.

[11] M. Sung, G. Zangari, M. Shamsuzzoha, and R. M. Metzger, "Electrodeposition of highly uniform magnetic nanoparticle arrays in ordered alumite," *Appl. Phys. Let.*, vol. 78, pp. 2964–2967, 2001.

[12] P. T. Tang, "Pulse reversal plating of nickel and nickel alloys for microgalvanics," *Electrochim. Acta*, vol. 47, pp. 61–66, 2001.

[13] H. Natter and R. Hempelmann, "Nanocrystalline copper by pulse electrodeposition: The effect of organic additives, bath temperature and pH," *J. Phys. Chem.*, vol. 100, pp. 19 525–19 532, Dec. 1996.

[14] T. R. Rosebrugh and W. L. Miller, "Mathematical theory of the changes of concentration at the electrode brought about by diffusion and by chemical reaction," *J. Phys. Chem.*, vol. 14, pp. 816–885, 1910.

[15] H. Schultz and M. Pritzker, "Modeling the galvanostatic pulse and pulse reverse plating of nickel-iron alloys on a rotating disk electrode," *J. Electrochem. Soc.*, vol. 145, pp. 2033–2042, Jun. 1998.

[16] D. T. Schwartz, B. G. Higgins, P. Stroeve, and D. Borowski, "Mass transfer studies in a plating cell with a reciprocating paddle," *J. Electrochem. Soc.*, vol. 134, pp. 1639–1645, Jul. 1987.

[17] L. Pauling, *College Chemistry*, 3rd ed. London, U.K.: W. H. Freeman, 1964, p. 445.

[18] G. Prentice, *Electrochemical Engineering Principles*. Englewood Cliffs, NJ: Prentice Hall, 1991, p. 269.

[19] C. Wagner, "Theoretical analysis of the current density distribution in electrolytic cells," *J. Electrochem. Soc.*, vol. 98, pp. 116–128, Mar. 1951.

[20] S. R. Brankovic, N. Vasiljevic, T. J. Klemmer, and E. C. Johns, "Influence of additive adsorption on properties of pulse deposited CoNiFe alloys," *J. Electrochem. Soc.*, vol. 152, pp. C196–C202, 2005.

[21] C. Buess-Herman, *Adsorption of Molecules at Metal Electrodes*, J. Lipkowski and P. N. Ross, Eds. New York: VCH, 1992, p. 80.

[22] H. Hoffmann and T. Fujii, "The wall coercivity of soft magnetic films," *J. Magn. Magn. Mater.*, vol. 128, pp. 395–400, 1993.

[23] H. H. Uhlig, *The Corrosion Handbook*. New York: Wiley, 1947, p. 125.

[24] G. Kresse and J. Furthmüller, "Efficient iterative schemes for *ab initio* total-energy calculations using a plane-wave basis set," *Phys. Rev. B*, vol. 54, pp. 11 169–11 175, 1996.